Article

Philippine archipelago and South China Sea monsoon plus ocean cooling buffer Northwestern Pacific super typhoons

Tian Ma [1], Wei-Dong Yu [1,2,3] ✉, Sabrina Speich [4], Hai-Kun Zhao [5], Rui Xin[1], Hao Luo [6] & Li-Guang Wu[7]

In dramatic contrast to the continuous intensification of strong Atlantic hurricanes moving into the Gulf of Mexico, super typhoons (SuperTYs) originating from the Northwest Pacific significantly weaken after entering the South China Sea (SCS). Using an idealized cyclone intensity model, we show that this striking discrepancy results from the SCS's buffering effects, including persistent topographic blocking by the Philippine archipelago and seasonally shifting atmospheric–oceanic constraints. The archipelago accounts for ~54% of typhoon weakening throughout the season, while environmental factors explain the remaining ~46% with the significant seasonal dependence on strong SCS monsoon-induced vertical wind shear in summer (~30%) and ocean cooling in autumn (~37%). The Coupled Model Intercomparison Project Phase 6 projects that these buffering effects may likely persist through the 21st century. These findings enhance our understanding of the SCS coastal vulnerability to typhoon impacts, with broader implications for climate risk management.

The super typhoons (SuperTYs) cause huge impacts along their track and even extreme destructions in the coastal region once landing[1,2], which stands out dramatically from the tropical cyclones (TCs). While both the Northwest Pacific (WNP) and the North Atlantic (NA) regions are prone to SuperTYs (Fig. 1), SuperTYs from WNP consistently weaken after entering the South China Sea (SCS), while the NA hurricanes maintain their intensity or even get intensified after entering the Gulf of Mexico (GM). The probability of the SuperTY occurrence in SCS is significantly lower (4.3%) compared to that in GM (17.3%). Thus, the SCS can be regarded as a natural "buffer"[3] that protects the adjacent coastline from the destructive impact of SuperTYs, whereas the US coast is more exposed to SuperTY risks. Gaining insight into the

underlying mechanisms responsible for this buffering effect is crucial for improving operational forecasting and assessing future typhoon disaster risks. However, SCS buffering effect and the SCS-GM contrast remain poorly understood.

The theoretical framework for assessing TC intensity has predominantly centered around the Maximum Potential Intensity (PI) theory, which estimates the theoretical maximum intensity that a TC can reach[4,5]. According to PI theory and most high-resolution climate models, TCs are expected to intensify as sea surface temperature (SST) warm under global warming[6–13]. However, the regional response in TC intensity to warming ocean varies significantly[14]. For instance, the no significant trend of TC intensity in the SCS diverges from the rising

[1]School of Atmospheric Sciences, Sun Yat-sen University, 519082 Zhuhai, China. [2]Southern Marine Science and Engineering Guangdong Laboratory, 519082 Zhuhai, China. [3]Guangdong Province Key Laboratory for Climate Change and Natural Disaster Studies, Sun Yat-Sen University, 519082 Zhuhai, China. [4]Department of Geosciences, Laboratoire de Météorologie Dynamique, École Normale Supérieure, 75231 Paris, France. [5]State Key Laboratory of Climate System Prediction and Risk Management/Key Laboratory of Meteorological Disaster, Ministry of Education/Collaborative Innovation Center on Forecast and Evaluation of Meteorological Disasters, Nanjing University of Information Science and Technology, 210044 Nanjing, China. [6]Leipzig Institute for Meteorology, Leipzig University, 04103 Leipzig, Germany. [7]Department of Atmospheric and Oceanic Sciences and Institute of Atmospheric Sciences, Fudan University, 200438 Shanghai, China. ✉e-mail: yuwd@mail.sysu.edu.cn
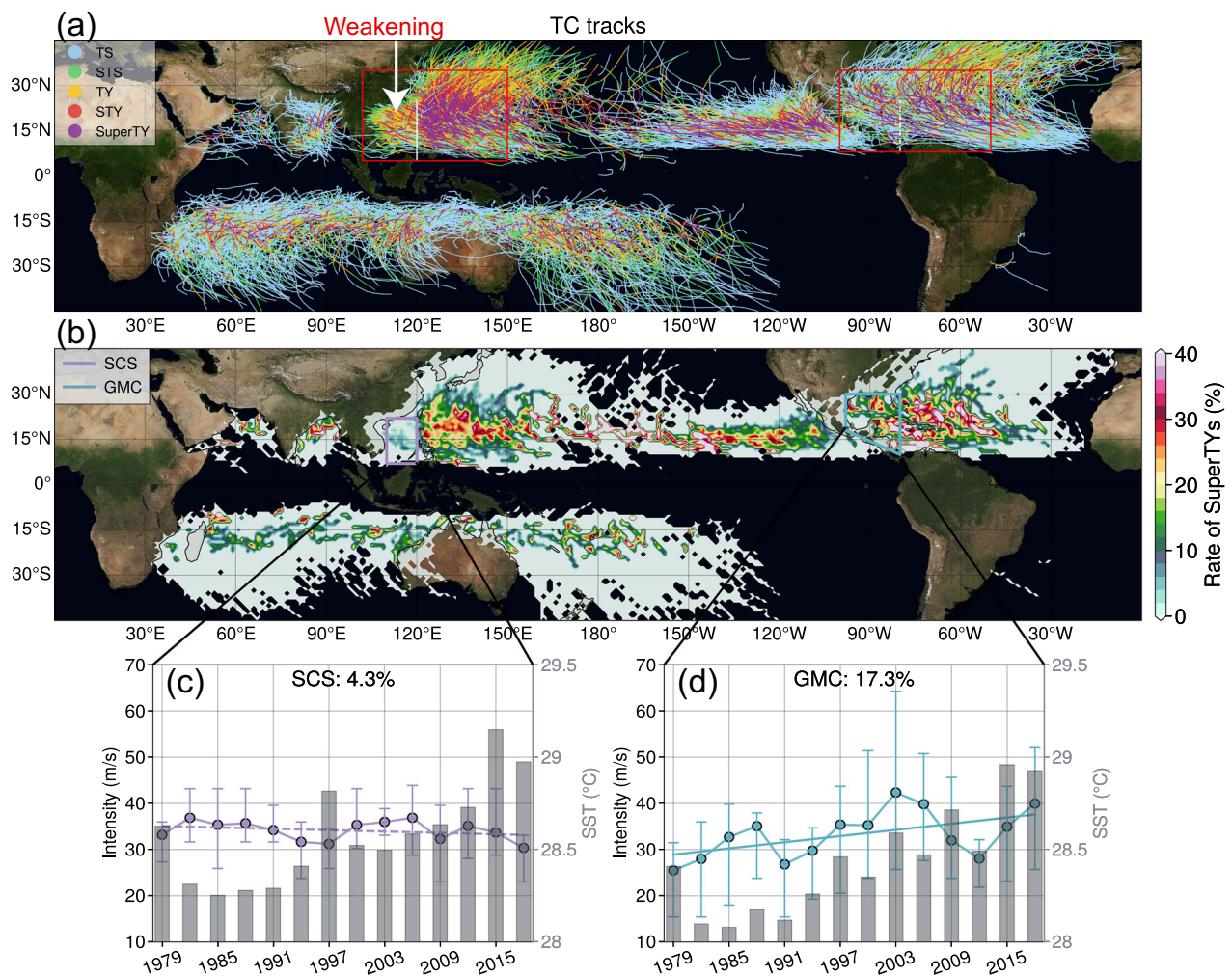
Fig. 1 | Global distribution of tropical cyclones (TCs) and regional contrasts. **a** Global TC tracks from 1979−2020, with intensity indicated by color categories: tropical storm (TS; 17−24.4 m s⁻¹), severe tropical storm (STS; 24.5−32.6 m s⁻¹), typhoon (TY; 32.7−41.4 m s⁻¹), severe typhoon (STY; 41.5−51 m s⁻¹), and super typhoon (SuperTY; ≥51 m s⁻¹). Red boxes denote the regions selected for comparative analysis. **b** Spatial distribution of SuperTY occurrence rate (%), calculated as the proportion of SuperTY points relative to all TC points within each 1° × 1° grid cell. **c, d** Interannual variations in TC intensity (colored dots, m s⁻¹) and mean sea surface temperature (SST, bars, °C) in the South China Sea (SCS) and the Gulf of Mexico plus part of the Caribbean Sea (GMC) during the boreal summer and autumn. TCs that remained in the regions for at least 1 day were included. TC intensity was calculated as the maximum intensity of each TC within the region and then averaged over all TCs in each 3 year period, with error bars showing the 25th and 75th percentiles. Solid (Dotted) lines show statistically significant (non-significant) linear trends at a 95% confidence level. Numbers in the titles denote the percentage of SuperTYs in each region. [Inspired by Fig. 1 in ref. 26].

trend in the GM (Fig. 1c, d). This regional contrast suggests that other environmental factors, such as upper-ocean thermal structure[15–19], vertical wind shear[20–23], and mid-tropospheric humidity[24], may play significant roles in influencing TC intensity. Yet, the relative importance of these factors under different regional conditions remains unclear[25].

While the SCS buffering effect was initially proposed based on statistical analyses of typhoons crossing the Luzon Strait[3], that work focused on northern SCS storms and emphasized interdecadal variability. A recent study[26] broadened the scope to the entire basin and provided substantial mechanistic insight, highlighting the amplifying effect of strong internal tides on SST cooling that suppresses TC intensification. Notably, SuperTYs such as Typhoon Megi[27] have been observed to weaken when crossing the Philippine terrain. This aligns with the sharp intensity drop near 120°E, suggesting a topographic constraint that has yet to be quantitatively assessed relative to the environmental background.

This study aims to advance understanding of the SCS buffering effect by quantitatively separating the roles of large-scale environmental fields and topographic constraints. We first investigated the relatively unfavorable environmental factors within the SCS and analyzed the underlying processes through cross-basin comparisons. We then quantified the respective contributions of the Philippine archipelago and environmental fields using idealized tropical cyclone model simulations. Finally, we assess the potential future evolution of the buffering effect under climate change based on CMIP6 multi-model projections.

Results

Severe typhoons over the South China Sea

Figure 2a, b illustrate the distribution of SuperTYs during the boreal summer and autumn, with a specific focus on those entering the SCS. Although the number of westward SuperTYs is relatively limited, with 9 out of 65 in summer and 28 out of 115 in autumn, they rarely dissipate in the open sea, resulting in considerable economic losses and casualties in the surrounding areas of the SCS. Typically, these typhoons reach their maximum intensity in the eastern Philippines and subsequently weaken after crossing the Philippines and the Luzon Strait into the SCS.

Focusing on the most intense typhoons affecting the SCS, the majority of those reaching severe or super typhoon (STY or SuperTY)
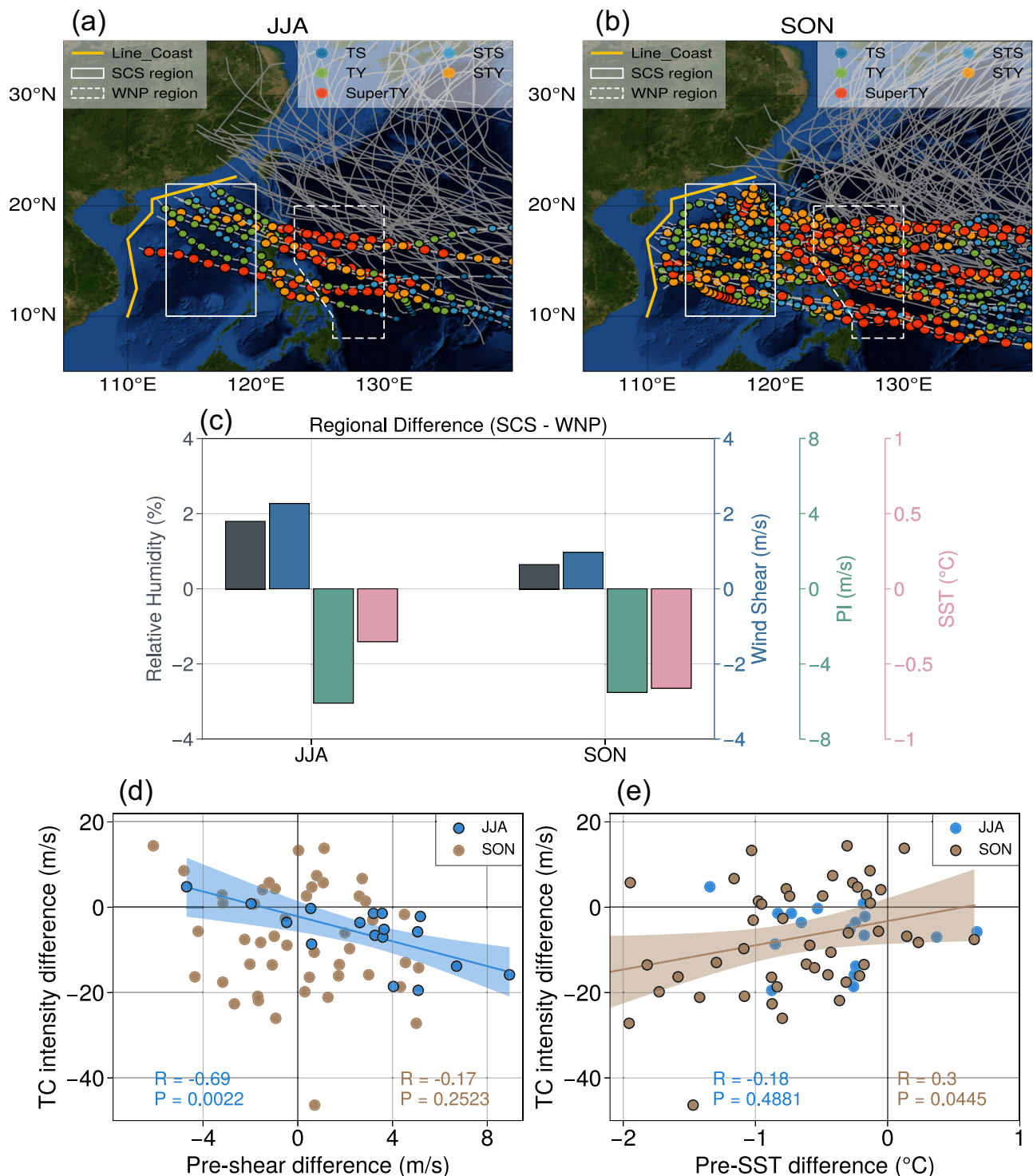
Fig. 2 | Seasonal variations in super typhoon (SuperTY) occurrence and Northwest Pacific typhoon (WNPTY) intensity with environmental differences. a, **b** Colored tracks indicate SuperTYs that entered the South China Sea (SCS, white solid box) and remained for at least 1 day during the boreal summer (June–August, JJA) and autumn (September–November, SON). Gray tracks represent SuperTYs that did not meet this criterion. Colored dots show the tropical cyclone (TC) intensity category: tropical storm (TS), severe tropical storm (STS), typhoon (TY), severe typhoon (STY), and super typhoon (SuperTY). **c** Climatological differences in TC environmental factors between the SCS and Northwest Pacific (WNP, white dashed box); see Methods for detailed calculations of environmental factors. **d** Linear correlation between mean difference (SCS minus WNP) in pre-TC wind shear (pre-shear, m s⁻¹) and the corresponding WNPTY intensity difference (m s⁻¹) during summer (blue) and autumn (brown). WNPTY sample selection is described in the Methods. Each pre-shear value is averaged within a 350 km radius of the TC center and from 15–3 days before the TC observation. The solid line indicates the linear regression, with Pearson correlation coefficient (R) and significance level (P) labeled. The shaded area denotes the 95% confidence interval. **e** Same as (**d**) but for pre-TC sea surface temperature (SST, °C).

intensity within the SCS originate east of 130°E, accounting for 64.6% for STYs and 77.8% for SuperTYs (Fig. S1). In contrast, locally generated TCs within the SCS tend to exhibit lower intensity. This high-risk group originating east of 130°E, comprising 64 TCs, forms the primary focus of our subsequent analysis and is hereafter referred to as Northwest Pacific typhoons (WNPTYs; see Methods for selection criteria). The pronounced weakening of these WNPTYs upon entering the SCS underscores the region's buffering effect against strong typhoons, likely influenced by the Philippine archipelago's blocking role and the contrasting large-scale environmental conditions between the SCS and WNP[3,26,28].

The dominant environmental factors influencing the WNPTYs

The buffering effect of the SCS against WNPTYs can reasonably be attributed to its relatively unfavorable environmental conditions. Figure 2c compares key environmental factors relevant to TC development between the SCS and WNP, including vertical wind shear, relative humidity, PI, and SST. The SCS exhibits stronger vertical wind shear and weaker PI compared to the WNP, particularly during the boreal summer. These atmospheric and oceanic conditions collectively limit the westward intensification of WNPTYs.

To quantify their relative influence, Fig. 2d, e examine the direct impact of these factors on WNPTY intensity changes. During summer, regional variations in vertical wind shear are the dominant driver, with a significant linear correlation coefficient of −0.69. In contrast, WNPTYs show limited sensitivity to regional SST differences. Larger pre-TC vertical wind shear differences result in more pronounced weakening of WNPTYs, while negative differences can even lead to their strengthening. Strong vertical wind shear disrupts the structure of TCs, hindering upward motion and energy concentration within the cyclone[21,29–33].

These regional differences are largely shaped by the South China Sea Summer Monsoon (SCSSM), which weakens from west to east (Fig. S2a). During the summer monsoon, intensified southwesterly winds in the lower atmosphere and northeasterly winds in the upper atmosphere increase vertical wind shear. The stronger low-level southwesterly winds and deep convection significantly reduce the SST through processes such as enhanced entrainment, latent heat release, and blocked short-wave radiation. The zonal gradients in vertical wind shear and SST induced by the summer monsoon, particularly the former, hinder the westward development of WNPTYs. The Bay of Bengal offers an even more extreme case, where the stronger vertical wind shear entirely prevents the formation of SuperTYs[34].

After the SCSSM, the vertical wind shear and its zonal gradient rapidly decrease, reducing the atmospheric dynamical constraints on WNPTYs. Meanwhile, the faster cooling of the SCS enhances the thermal constraints on WNPTYs. As a result, WNPTYs become increasingly sensitive to oceanic thermal conditions (Fig. 2e). During the transitional window from the summer to winter monsoon, the combination of reduced vertical wind shear and SSTs remaining above 28 °C creates favorable conditions that make the SCS more susceptible to strong typhoons[35,36].

In contrast, the environmental factors in the North Atlantic trade wind region exhibit an east-west gradient opposite to that in the monsoon region (Fig. S2b). Easterly winds in the lower atmosphere and vertical wind shear decrease from east to west, while SST increase in the same direction. Additionally, both circulation patterns and SST follow a unimodal structure, peaking in September. As a result, hurricanes in the GM and the Caribbean Sea are most frequent in September[37], and generally intensify as they move westward (Fig. S3). The GM's atmospheric and oceanic conditions, including weaker vertical wind shear, warmer SST, and higher mid-tropospheric humidity, collectively favor hurricane intensification during the peak season.

A previous study[26] identified the SCS as a relatively favorable TC environment based on global basin comparisons, and accordingly emphasized strong TC-induced SST cooling as a key suppression mechanism. In contrast, our analysis focuses specifically on WNPTYs. In this context, the SCS exhibits comparatively unfavorable atmospheric–oceanic conditions relative to the WNP. To enable a consistent cross-basin comparison, we further evaluate environmental conditions across major Northern Hemisphere TC basins (Fig. S4). The results confirm that the SCS exhibits stronger pre-TC vertical wind shear during the summer monsoon (JJA), while its TC-induced SST cooling becomes particularly pronounced during autumn (SON), approaching that in the GM. Nonetheless, the GM has higher pre-TC SSTs, providing more favorable thermal conditions for TC intensification. In contrast, the SCS shows no seasonal advantage in either summer SST cooling or autumn wind shear.

These results suggest a seasonally complementary buffering structure in the SCS for strong WNPTYs, with summer dominated by atmospheric dynamical suppression and autumn by oceanic thermal suppression. However, environmental constraints alone may not fully account for the sharp intensity drop observed near 120°E, motivating further investigation into the role of the Philippine archipelago.

## Mechanistic quantification of topographic and environmental buffering

The meridional topography of the Philippine archipelago on the eastern side of the SCS contrasts with the conditions in the GM. To assess its buffering effect on WNPTYs, we employed a tropical cyclone intensity model[38]. Since the original model did not account for tropical cyclones passing over islands, we added a 'Philippine archipelago' module. The modified simulation, which includes this module, serves as the control experiment (Experiment 0, EX0). For comparison, the original model, where the Philippine Islands were removed, represents the alternative experiment (EX1). Details of the experimental design are provided in the Methods section. The validation results are shown in Fig. S5, where EX0 accurately reproduces the intensity changes of WNPTYs east of the Philippines. Although there are some deviations over the archipelago, the model's accuracy is restored west of 117°E, providing confidence in subsequent comparisons.

The results from EX1 suggest that without the Philippine archipelago, the peak intensity of WNPTYs would shift westward to 120°E, leading to a notable increase in both the average intensity and frequency of SuperTYs within the SCS. As WNPTYs progress further into the SCS, they weaken due to the influence of environmental gradients.

Figure 3 evaluates the buffering impact of the Philippine archipelago on WNPTYs by comparing their intensity at two key locations. The first location is set to the east of the Philippines (green line), where WNPTYs typically reach their peak intensity. The second is near the northwest coastline of the SCS (yellow line). Both observations and EX0 show a similar intensity reduction between these two points (−−8.3 m s⁻¹). This reflects the combined buffering effects of the Philippine archipelago and the SCS environmental conditions.

When the archipelago is removed (EX1), the reduction shrinks to -3.8 m s⁻¹. Taking EX0 as the baseline (100% total weakening), this implies that SCS atmospheric–oceanic conditions (e.g., wind shear and upper-ocean thermal structure) alone explain 46%, whereas the Philippine archipelago contributes 54% ± 5.3% (90% confidence interval, based on $\alpha_{max} = 35\%$–55% sensitivity tests shown in Fig. S6). The same two-location comparison yields nearly identical results in both summer and autumn (46%/54% vs. 45%/55%).

To assess the influence of empirically parameterized shear, we conducted sensitivity experiments, which show that the buffering attribution remains robust under varying shear formulations (Table S1). We also extended the analysis to explicitly assess the mechanism of enhanced TC-induced SST cooling, inspired by the observational evidence reported by a previous study[26]. By introducing a flux adjustment factor based on amplified cooling magnitudes ranging from 1 × to 5 × (see Methods), our sensitivity experiments (Fig. S7)
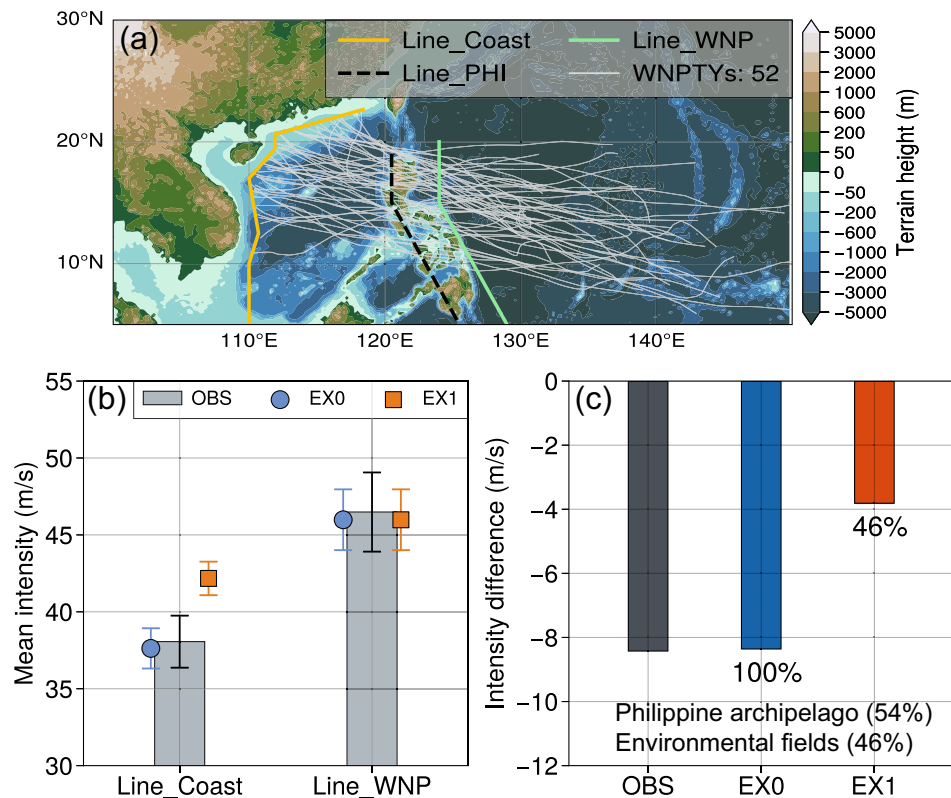
Fig. 3 | The contribution of the Philippine archipelago to the buffering effect. **a** Terrain height (m) of the East Asian region. White lines indicate the tracks of Northwest Pacific typhoons (WNPTYs; see Methods) that crossed the yellow coastline. **b** The mean intensity (m s⁻¹) of WNPTYs during the half-day before reaching the Northwest Pacific (WNP) line (Line_WNP) and the coastline (Line_-Coast). Error bars indicate the 90% confidence interval. 'OBS', 'EX0', and 'EX1' represent the observations, the control experiment, and the experiment in which the Philippine archipelago was removed, respectively (see Methods for details). **c** The difference in the mean intensity (m s⁻¹) of WNPTYs between the coastline and the WNP line. In this study, the intensity difference in EX0 is set as 100%, representing the total buffering effect. The 46% in EX1 represents the relative contribution of atmospheric–oceanic conditions, while the remaining 54% is attributed to the Philippine archipelago, as noted below the bars.

show that even under enhanced cooling conditions, the relative contributions of the environmental field and the Philippine archipelago remain comparable (41%/59%), with the environmental contribution slightly increasing during autumn (52%, compared to 45% in the baseline case). This underscores the archipelago's irreplaceable role in suppressing WNPTYs.

A seasonal decomposition (Table S2) further quantifies the previously suggested seasonal complementary of atmospheric–oceanic conditions by explicitly isolating vertical wind shear (EX2; see Method), which maintains fixed shear values after the storm crosses Line_WNP. During summer and autumn, vertical wind shear accounts for $30 \pm 4\%$ and $8 \pm 3\%$ of the typhoon weakening, respectively, while the residual oceanic component contributes 16% and 37%, respectively. Uncertainty estimates reflect sensitivity only to the shear parameter.

It's important to note that the above experiments did not account for the influence of terrain elevation, particularly the Cordillera Central mountains in northern Philippines. To further assess the role of topographic height in modulating SuperTY intensity, we conducted additional sensitivity experiments using the Weather Research and Forecasting (WRF) model. As detailed in the Methods section, a total of 11 observed SuperTYs that crossed the Cordillera Central were simulated, of which four were retained for detailed analysis based on their agreement with observed intensity and track.

Across all four cases, reducing terrain elevation to 15 m or 1 m resulted in minimal changes in intensity compared to the control runs, indicating that the elevation of the Cordillera Central had limited influence (Fig. S8), consistent with a previous case study[27]. In contrast,

complete removal of the Philippine archipelago consistently led to markedly stronger typhoons downstream, reaffirming the buffering role of the islands as a whole.

Notably, both the land module in the WRF model and the simplified 'Philippine archipelago' module in the modified tropical cyclone intensity model amplify the weakening effect of the archipelago on super typhoons. This highlights that the complex processes induced by islands remain inadequately understood. In contrast to the growing focus on rapid the intensification of SCS TCs[36,39,40], these underexplored blocking effects are likely to be equally crucial for operational forecasting, as they determine the initial state of WNPTYs upon entering the SCS, which in turn influences their subsequent intensification. This underscores the need for further research into these processes to enhance the accuracy and reliability of operational forecasts.

Future evolution of the buffer zone

Assessing trends in TC activity in the context of climate change presents a significant challenge and remains controversial due to the confounding effects of natural variability and the limited availability of long-term observations. Several studies[14,41–46] indicate that the most significant trend observed in the WNP is a poleward shift in TC tracks, rather than an increase in the frequency of intense typhoons. However, projections from numerous studies suggest that the frequency of very intense TCs is expected to increase as global warming progresses[6–13]. This raises a critical question: Will the SCS buffering effect continue to mitigate the risk of SuperTYs in surrounding regions under future anthropogenic warming?
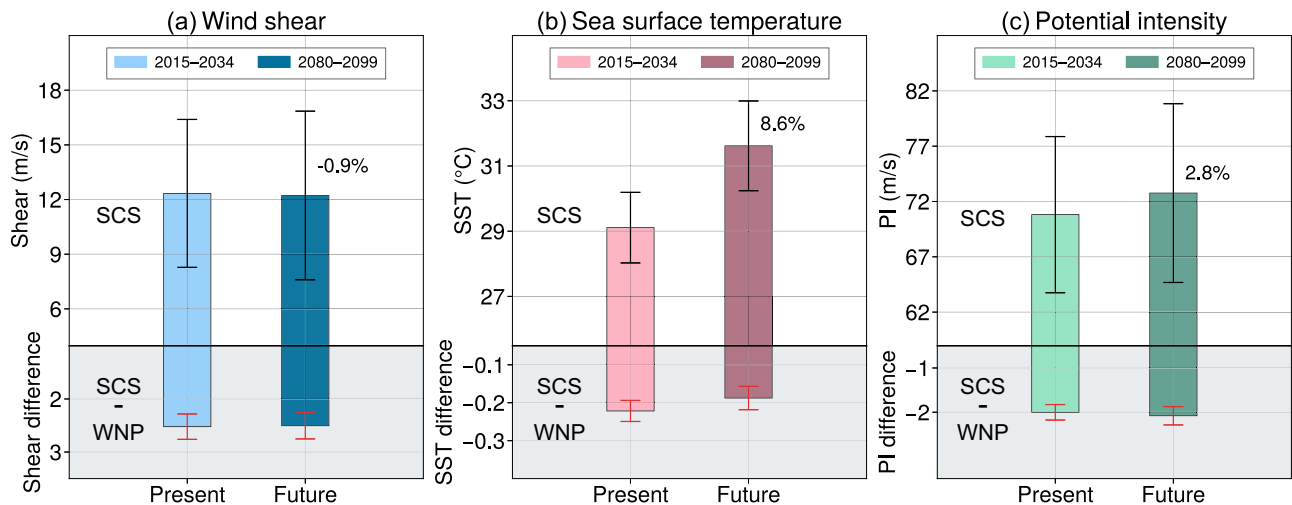
Fig. 4 | Projected changes in tropical cyclone environmental factors under severe anthropogenic warming scenarios. a Upper panels show the vertical wind shear (m s⁻¹) over the South China Sea (SCS, white solid box in Fig. 2a) during the boreal summer and autumn for the current 20 years (2015–2034) and the future 20 years (2080–2099), with error bars representing the multi-model standard deviation over 20 years. The numbers indicate the change rate in the mean values.

Lower panels (gray shading) show the regional differences between the SCS and the Northwest Pacific (WNP, white dashed box in Fig. 2a), with error bars representing the 90% confidence interval. **b**, **c** Same as (**a**), but for sea surface temperature (SST, °C) and potential intensity (PI, m s⁻¹), respectively. Under the Shared Socioeconomic Pathway 5-8.5 (SSP5-8.5) scenario, the selected Coupled Model Intercomparison Project Phase 6 (CMIP6) multi-models are listed in Table S3.

To predict future changes in SuperTY activities, two primary methods are employed[11,47,48]: (1) dynamical downscaling and (2) the use of TC development-related indices. The first approach offers a more direct prediction of future TC changes. Simulation results for Super-TYs in the WNP are promising, but the same cannot be stated for the SCS[49]. Therefore, as an alternative approach, we analyze the large-scale environmental factors in this study using multi-model ensembles from the Coupled Model Intercomparison Project Phase 6 (CMIP6). This allows us to infer indirectly whether the SCS's natural buffering effect will persist under anthropogenic warming.

Figure 4 illustrates changes in WNPTY environmental factors under the most extreme anthropogenic warming scenario. One of the key factors during summer, the SCS vertical wind shear and its east-west gradient, shows little change in the ensemble mean. The SST is expected to increase significantly, by ~2.5 °C (8.6%), while the corresponding rise in PI is more modest (2.8%). This is largely because the potential increase in TC intensity is counterbalanced by the simultaneous warming of the upper troposphere in a high-CO₂ climate[50,51]. A 2.5 °C rise in SST alone would substantially elevate the risk of intense typhoons within the buffer zone (Fig. S9). However, previous WRF experiments suggest that when accounting for concurrent changes in atmospheric temperature and relative humidity, the impact of the SST increase is significantly diminished, resulting in little change in WNPTY intensity[51].

It is anticipated that the effectiveness of the buffer zone may persist through the end of this century, particularly during the summer monsoon season. This projection is based on several relatively stable factors: the presence of the Philippine Islands, the relatively unchanged vertical wind shear, and the modest increase in PI, even under extreme warming scenarios. Observational evidence further supports this view: despite significant regional SST warming, SCS typhoon intensity has shown no clear upward trend in recent decades, likely due to stable shear (Fig. S10) and strong TC-induced ocean cooling[26].

However, this conclusion remains conditional. It is derived from trends in a limited set of large-scale proxies that may not capture finer-scale physical processes such as island-induced disruptions and air–sea coupling. Ensemble variance of these environmental fields also increases under warming (Fig. 4), contributing further uncertainties.

Moreover, seasonal asymmetry may emerge if SSTs continue to rise (Fig. S9): vertical shear in summer may offset warming effects, while autumn conditions could favor more intense typhoons.

Discussion

Our study advances the understanding of the South China Sea buffer zone by quantitatively attributing the weakening of strong WNPTYs to the respective roles of the Philippine archipelago and atmospheric–oceanic constraints (Fig. 5). Using an idealized cyclone intensity model, we identify the Philippine archipelago as a robust geometric barrier, accounting for ~54% ± 5% of typhoon weakening across the entire typhoon season. In contrast, atmospheric–oceanic constraints contribute the remaining 46%, displaying pronounced seasonal variability.

During summer, strong vertical wind shear induced by the South China Sea monsoon emerges as the primary environmental inhibitor for strong WNPTYs, responsible for about 30 ± 4% of the weakening. This result helps clarify previous inconsistencies regarding shear effects[3,26,35,36], emphasizing that significant suppression primarily affects stronger typhoons, while weaker storms remain less influenced (Fig. S4). With the weakening of shear in autumn, the primary environmental control shifts towards oceanic conditions, which account for ~37% of the typhoon weakening. This finding quantifies the seasonal role of the previously proposed SST cooling mechanism[26], confirming its importance in autumn, but showing that topographic blocking remains indispensable (Fig. S7). Thus, the total buffering effect is maintained by a seasonally shifting balance between atmospheric and oceanic constraints, superimposed on a persistent topographic barrier, jointly enhancing the robustness of the SCS as a natural buffer zone against super typhoon impacts. In contrast, the GM lacks similar meridional island barriers, and its environmental gradients instead favor westward intensification, resulting in more frequent super hurricanes.

We explicitly isolated the effects of topography and wind shear through targeted experiments and assessed their uncertainties using sensitivity tests on the island flux-reduction parameter and shear coefficients. While these efforts provide a solid foundation for our quantitative attribution, several sources of uncertainty remain. As a residual term, the oceanic contribution may encompass
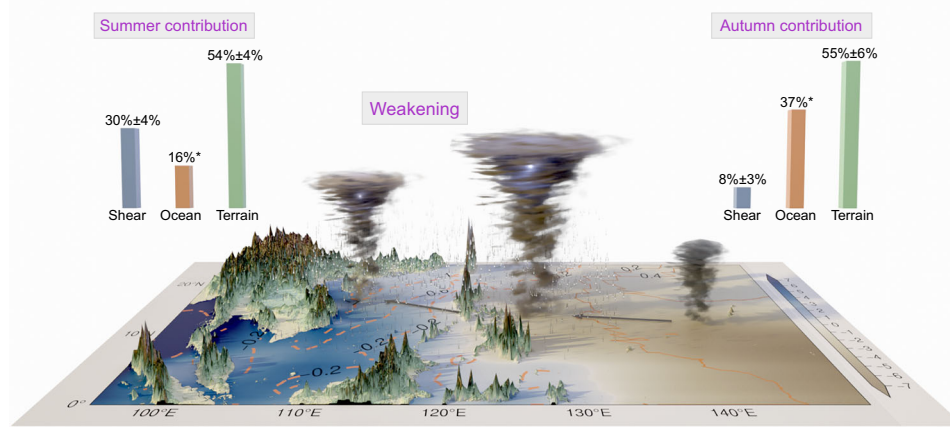
Fig. 5 | Schematic illustration of the South China Sea (SCS) buffering effect and seasonal attribution. Shading shows the summer-mean vertical wind shear anomaly (m s^{-1}, relative to the zonal average), while contours indicate autumn sea surface temperature anomaly (°C, relative to the zonal average). The 3D structure represents idealized typhoon weakening across the SCS. Bar charts illustrate the seasonal contributions to typhoon weakening from monsoon shear (blue), ocean cooling (orange), and Philippine archipelago's topographic blocking (green) during summer and autumn, based on the quantitative decomposition results shown in Table S2. Oceanic contributions (marked by asterisks) are inferred as residuals after isolating the effects of shear and topography.

unquantified influences, including unrepresented interactions among atmospheric, oceanic, and topographic processes. Similar limitations also exist in the uncoupled WRF simulations employed here, which do not capture dynamic SST cooling, sub-surface feedback, or prior-storm memory effects—all of which are important for realistically simulating typhoon intensity changes. Additionally, summer monsoon-driven track shifts, which may steer typhoons northward, were not explicitly quantified and likely contribute to the observed seasonal differences. These limitations do not alter our core findings, but they highlight the need to further advance coupled atmosphere–ocean–terrain modeling frameworks to improve the completeness and accuracy of future attribution analyses.

Looking ahead, CMIP6 multi-model projections suggest that the SCS buffer zone may continue to moderate SuperTY risk through the 21st century, supported by relatively stable topography, wind shear and potential intensity. However, this conclusion remains conditional, as it relies on trends in a limited set of large-scale proxies that cannot fully represent finer-scale processes like island-induced disruptions, internal tides, and detailed air–sea coupling. Moreover, increased variance across CMIP6 models under warming scenarios reflects enhanced uncertainty (Fig. 4), potentially driven by either inter-model differences or a true increase in internal climate variability. In the latter case, the SCS could face intensified typhoon activity during particularly extreme years. Additionally, future typhoon risks will likely depend on shifts in monsoon circulation driven by uneven warming[47,52], which may alter storm tracks even without substantial changes in storm intensity[53]. While the SCS may remain more resilient[54] than temperate regions such as eastern China and Japan[55,56], this buffering is conditional and shaped by processes not fully resolved in current climate models.

While our study provides a foundation for long-term assessments of extreme typhoon hazards in the SCS buffer zone, it also highlights considerable challenges in short-term operational forecasting, as current high-resolution regional models struggle to accurately capture these island-forcing effects (Fig. S8), revealing gaps in understanding the complex influence of topography in TC behavior. Similar island-induced blocking effects may also play a crucial role in other cyclone-prone regions, such as the Taiwan Strait and the Mozambique Channel. Addressing this gap is crucial for improving operational TC forecasts, extending lead times, and ultimately enhancing disaster preparedness and response strategies.

Methods

Data

TC tracks and intensity information are obtained from the World Meteorological Organization (WMO) subset of the International Best Track Archive for Climate Stewardship (IBTrACS-WMO) version 4, which uses data from the official WMO agency in each region. IBTrACS is the most comprehensive global collection of tropical cyclone data currently available. It combines current and historical tropical cyclone data from several agencies, including the Joint Typhoon Warning Center (JTWC), WMO Regional Specialized Meteorological Centers (RSMCs), Tropical Cyclone Warning Center (TCWC), and the Shanghai Typhoon Institute[57].

The large-scale environmental factors related to TCs mainly include (a) monthly and daily wind, air temperature, relative and specific humidity, and sea level pressure from the European Centre for Medium-Range Weather Forecasts (ECMWF) Reanalysis v5 (ERA5)[58], (b) Sea Surface Temperature (SST) obtained from NOAA high-resolution SST data products (OISST)[59], (c) Mixed-layer depth (MLD) obtained from the NCEP Global Oceanographic Data Assimilation System (GODAS). In addition, we analyzed 43 model simulations from the Coupled Model Intercomparison Project Phase 6 (CMIP6)[60]. These include the latest generation of integrated Earth System Models (ESM), driven by historical greenhouse gas concentrations. Each scenario simulation in CMIP6 is run under a combination of the Representative Concentration Pathways (RCP) and Shared Socio-Economic Pathways (SSP)[61]. The most extreme scenario (SSP5-8.5) was selected for this study (Table S3).

Basemap imagery (e.g., in Fig. 1a) was obtained from the NASA Moderate Resolution Imaging Spectroradiometer (MODIS) Blue Marble dataset (August 2004), provided by the NASA Earth Observatory. Global topographic elevation data were obtained from the NOAA 15 arc-second Global Relief Model (TOPO15).

Tropical cyclone classification

With reference to the global tropical cyclone classification from IBTrACS[57], we categorize typhoon intensity (maximum sustained winds, MSW) as follows: tropical storms (TS, 17 m s^{-1} ≤ MSW < 24.5 m s^{-1}), severe tropical storms (STS, 24.5 m s^{-1} ≤ MSW < 32.7 m s^{-1}), typhoons (TY, 32.7 m s^{-1} ≤ MSW < 41.5 m s^{-1}), severe typhoons (STY, 41.5 m s^{-1} ≤ MSW < 51.0 m s^{-1}), and super typhoons (SuperTY, MSW ≥ 51.0 m s^{-1}). A SuperTY is roughly equivalent to a Category 3 to 5 hurricane on the Saffir-Simpson scale. The IBTrACS-WMO dataset includes MSW

measurements from various agencies. Following previous studies[62,63], we converted certain 10 min average wind speed data in the dataset to 1 min average wind speed by dividing by a factor of 0.88.

Calculation of large-scale environmental factors on TCs

Vertical wind shear is the difference in wind speed between two atmospheric levels. It is calculated as:

$$\text{Vertical Wind Shear} = \sqrt{(U_{850} - U_{200})^2 + (V_{850} - V_{200})^2} \quad (1)$$

where U_{850} (V_{850}) and U_{200} (V_{200}) are the zonal (meridional) wind components at 850 hPa and 200 hPa. In addition, the relative humidity (RH) at 600 hPa is used to represent mid-tropospheric humidity.

The maximum potential intensity (PI) defined by ref. 64 and developed by refs. 65,66:

$$V_{\max}^2 = \frac{C_k}{C_D} \frac{T_s - T_o}{T_o} (h_o{}^* - h^*) \quad (2)$$

where C_k and C_D are the surface enthalpy momentum exchange coefficients; T_s and T_o are the sea surface temperature and outflow temperature; $h_o{}^*$ and h^* are the saturation moist static energy at the sea surface and at the free atmosphere respectively.

Selection criteria of TC tracks

In this study, TCs with a maximum intensity below $17\,\text{m s}^{-1}$ are first excluded from the analysis. Starting from Fig. 2d, this study focuses on the high-risk typhoon group impacting the SCS, defined as Northwest Pacific typhoons (WNPTYs), which originate from the WNP east of 130°E. The criteria selected for WNPTYs are as follows:

- TCs originate east of 130°E and reach their maximum intensity during the boreal summer and autumn.
- TCs cross the WNP region (white dashed box in the Fig. 2a) and enter the SCS (white solid box), where they remain for at least 1 day.
- The portion of TCs that crosses the yellow line (Fig. 2a) is excluded. This criterion is designed to minimize the potential influence of the eventual landfall.

Following these selection criteria, a total of 64 WNPTYs are identified, including 17 cases in summer and 47 in autumn. Among them, 52 TCs remain active upon reaching the northwestern boundary of the SCS (yellow line in Fig. 3a) and are thus included in the quantitative analysis of the buffering effect. Although not all tracks directly intersect the Philippine landmass, 84% cross the simplified representation of the archipelago (black dashed line in Fig. 3a), and the remaining cases pass within 90 km. This subset provides a representative basis for diagnosing the buffering effects of the SCS environment and the Philippine terrain.

Tropical cyclone intensity model

In this study, we verify the impact of Philippine topography on the buffer zone using a tropical cyclone intensity model. This model, adopted from previous studies[38,67], is an axisymmetric numerical atmospheric model coupled with a simple one-dimensional ocean model. In this study, the intensity model is initialized with a warm-core cyclonic vortex with a maximum wind speed of $21\,\text{m s}^{-1}$. The inputting environmental parameters include the daily vertical wind shear, SST, and ocean mixing layer depth (MLD). The MLD 's original data resolution is monthly average, which undergoes linear interpolation to derive daily values. All other fixed parameters follow the model's default configuration, except for the near-surface relative humidity, which is adjusted from 80% to 82% in this study to better reflect observed conditions over the South China Sea and the western North Pacific. Previous studies have shown that the model successfully

captured the interannual variability of TC intensity in the WNP, although it tends to overestimate the intensity[68,69]. This bias is reduced in our simulations through the adjustment of near-surface humidity.

The influence of islands was not considered by this model, which relies solely on the absence of SST data to determine TC landfall. The pre-TC input parameters, including vertical wind shear, SST, and MLD, are averaged within a 350 km radius of the TC center and over the period from 15–3 days prior to the TC observation point. In this way, the Philippine archipelago is replaced by the surrounding real marine and atmospheric environmental fields.

To evaluate the influence of the Philippine archipelago, an idealized "island module" was introduced. In this module, the TC's capacity to extract heat from the ocean is linearly reduced as the storm approaches a simplified representation of the archipelago (Fig. 3a, black dashed line). This reduction is governed by an empirical parameter α, which increases from 0 to a maximum value (αmax) as the TC moves from a distance of 350 km to 0 km from the island chain. Based on this setup, three primary experiments were conducted:

- Experiment 0 (EX0) serves as the control run, including the full island module (αmax = 45%), realistic wind shear, and oceanic inputs. It is calibrated to match the observed intensity weakening.
- Experiment 1 (EX1) removes the island effect (αmax = 0%) while keeping all environmental conditions unchanged. The difference between EX1 and EX0 isolates the contribution of topographic blocking by the Philippine archipelago.
- Experiment 2 (EX2) retains the island effect but fixes wind shear at its instantaneous value upon crossing Line_WNP (-123°E), thereby isolating the relative contribution of SCS wind shear.

The seasonal decomposition based on these three experiments is summarized in Table S2 and illustrated in Fig. 5, providing a clean partitioning of the total weakening into topographic, shear, and residual oceanic components.

Robustness testing of the island module. To test the robustness of our findings regarding the contribution of the Philippine archipelago, we performed additional sensitivity experiments using various αmax values (35%–55% in 5% intervals). These experiments defined a 90% confidence interval for the inferred buffering effect (Fig. S6).

Robustness testing of the shear parameterization. The tropical cyclone intensity model does not explicitly resolve the dynamic interaction between the storm and vertical wind shear. Instead, the shear effect is empirically parameterized as a function of the environmental sheer magnitude, with the default configuration assuming a quadratic dependence ($\sigma V_{\text{shear}}^2$, Equation (7) in the reference[38]), where σ is an empirically determined coefficient, and V_{shear} is the vertical wind shear. This parameterization is designed to capture the ventilating effect of environmental shear on the storm. Given this empirical treatment of shear, the robustness of the inferred buffering effect may depend on the specific form of this parameterization. To evaluate this potential sensitivity, we conducted additional experiments by modifying the shear dependence from quadratic to linear ($\sigma_1 V_{\text{shear}}$) and perturbing the parameterization coefficient by ±10% ($0.9\sigma_1$ and $1.1\sigma_1$). The results of these sensitivity tests are summarized in Table S1.

Robustness testing of the SST cooling amplification. A previous study[26] highlighted intensified SST cooling in the SCS due to internal tides interacting with TCs. Although our initial experiments accounted for the spatial variation of MLD, with shallower depths in the SCS enhancing TC cooling effects compared to the WNP, they might still have underestimated the extreme cooling observed in the SCS. Therefore, we conducted additional sensitivity experiments explicitly designed to assess the impact of amplified cooling effects.

This observed TC-induced SST cooling ($\Delta SST_{cooling}$) was quantified as the difference between the mean SST during day 0–1 after the observation point (SST1) and the pre-TC SST (SST0). Considering that cooling affects surface heat fluxes (thus modulating TC intensity), we introduced a flux ratio ($Q1/Q0$, Fig. S7a), which scales linearly with the SST cooling magnitude, and incorporated it into the model to represent amplified ocean cooling:

$$\text{flux ratio} = 0.04 \times \Delta SST_{cooling} \times \beta + 1 \qquad (3)$$

where β is a cooling amplification factor ranging from 1 (observed cooling) to 5 (amplified cooling). Considering that OISST may underestimate cooling compared to microwave observations[26], this factor compensates for potential data bias ($\beta = 2–3$ roughly corresponds to the adjusted $\Delta SST_{cooling}$ reported in that study). The linear relationship was estimated using the COARE 3.5 bulk flux algorithm[70], accounting for essential parameters such as SST, near-surface temperature (approximated as SST-1.4 °C), near-surface wind speeds and a unified near-surface relative humidity of 82%.

Using this relationship, we derived a *flux ratio* for each TC location, replacing the original MLD module in the model. The final outcomes of these sensitivity experiments are presented in Fig. S7b. Although this approach introduces some uncertainties, it explicitly accommodates the distinctively strong cooling effects observed in the SCS.

Weather Research and Forecasting (WRF) model

The tropical cyclone intensity model is relatively simple and idealized, making it difficult to assess the role of the Philippine terrain elevation. To address this, we further employed the WRF model to investigate the role of Philippine topography in modulating SuperTY intensity. We simulated 11 historical SuperTYs that crossed the northern Philippines.

The WRF simulations were performed using version 4.3.3 with three nested domains (27 km, 9 km, and 3 km horizontal resolution), with the innermost domain moving with the storm center. The model includes 45 vertical levels, extending to 20 hPa. Initial and boundary conditions were obtained from ERA5 hourly reanalysis. The physics configurations are summarized in Table S4. Extensive testing of various configurations and physical schemes indicates that the above configuration can capture the SuperTYs as effectively as possible.

Among the 11 simulated SuperTYs, only four reached super typhoon strength east of the Philippines, with peak intensity within ± 10 m s^{-1} of observations and reasonably aligned tracks, and were thus considered suitable for terrain sensitivity analysis. The remaining seven cases were excluded due to substantial intensity or track deviations. The selected cases—Elsie (1989), Nalgae (2011), Utor (2013), and Haima (2016)—were retained for further analysis.

For each of the four selected SuperTYs, we conducted a control run and three terrain sensitivity experiments: one with Philippine topography reduced to 15 m, another with elevation set to 1 m, and a final experiment in which the entire Philippine archipelago was removed and replaced by ocean. Sea surface temperatures in the removed-land experiment were filled using the average value within a 350 km radius surrounding the islands. All four storms passed over the Cordillera Central mountains, enabling a consistent assessment of elevation sensitivity across cases.

Figure S8 presents a representative example using Super Typhoon Utor (2013), covering the period from 00:00 UTC on August 10 to 12:00 UTC on August 13, encompassing both the intensification phase east of Luzon and the weakening phase after crossing the northern terrain. All four cases were included in the final intensity comparison to evaluate the relative contribution of topographic elevation versus the presence of the entire Philippine archipelago.

Data availability

The tropical cyclone best-track data are obtained from the National Centers for Environmental Information website (https://www.ncei.noaa.gov/products/international-best-track-archive). Atmospheric field data used for diagnostic analyses and WRF initialization are from ERA5 reanalysis (https://cds.climate.copernicus.eu/datasets). SST data are from NOAA OISST, and MLD data are from GODAS. CMIP6 model outputs are available at Earth System Grid Federation (ESGF, https://esgf-node.llnl.gov/search/cmip6/). The Blue Marble basemap imagery is available from the NASA GIBS Visualization Product Catalog (https://nasa-gibs.github.io/gibs-api-docs/available-visualizations/). Topographic elevation data (TOPO15) are available from the NOAA National Centers for Environmental Information (https://www.ngdc.noaa.gov/mgg/global/). All data used to generate the figures in this study are publicly available at Code Ocean (https://doi.org/10.24433/CO.1991288.v1).

Code availability

The codes used to generate the figures in this study are publicly available at Code Ocean (https://doi.org/10.24433/CO.1991288.v1).

References

1. Galvin, J. F. P. The development, track and destruction of Typhoon Haiyan. *Weather* **69**, 307–309 (2014).
2. Smith, A. B. *2020 U.S. Billion-dollar Weather And Climate Disasters In Historical Context*. https://www.climate.gov/disasters2020 (2022).
3. Sun, J., Oey, L., Xu, F.-H. & Lin, Y.-C. Sea level rise, surface warming, and the weakened buffering ability of South China Sea to strong typhoons in recent decades. *Sci. Rep.* **7**, 7418 (2017).
4. Emanuel, K. A. An air-sea interaction theory for tropical cyclones. Part I: steady-state maintenance. *J. Atmos. Sci.* **43**, 585–605 (1986).
5. Holland, G. J. The maximum potential intensity of Tropical Cyclones. *J. Atmos. Sci.* **54**, 2519–2541 (1997).
6. Manganello, J. V. et al. Future changes in the western north pacific tropical cyclone activity projected by a multidecadal simulation with a 16 km global atmospheric GCM. *J. Clim.* **27**, 7622–7646 (2014).
7. Wu, L. et al. Simulations of the present and late-twenty-first-century Western North Pacific Tropical Cyclone activity using a regional model. *J. Clim.* **27**, 3405–3424 (2014).
8. Yamada, Y. et al. Response of tropical cyclone activity and structure to global warming in a high-resolution global nonhydrostatic model. *J. Clim.* **30**, 9703–9724 (2017).
9. Choi, W., Ho, C.-H., Kim, J. & Chan, J. C. L. Near-future tropical cyclone predictions in the western North Pacific: fewer tropical storms but more typhoons. *Clim. Dyn.* **53**, 1341–1356 (2019).
10. Mei, W., Xie, S.-P., Primeau, F., McWilliams, J. C. & Pasquero, C. Northwestern Pacific typhoon intensity controlled by changes in ocean temperatures. *Sci. Adv.* **1**, e1500014 (2015).
11. Cha, E. J., Knutson, T. R., Lee, T.-C., Ying, M. & Nakaegawa, T. Third assessment on impacts of climate change on tropical cyclones in the Typhoon committee region—part II: future projections. *Trop. Cyclone Res. Rev.* **9**, 75–86 (2020).
12. Knutson, T. et al. Tropical cyclones and climate change assessment: part II: projected response to anthropogenic warming. *Bull. Am. Meteorol. Soc.* **101**, E303–E322 (2020).
13. Bloemendaal, N. et al. A globally consistent local-scale assessment of future tropical cyclone risk. *Sci. Adv.* **8**, eabm8438 (2022).
14. Sobel, A. H. et al. Tropical cyclone frequency. *Earth's Future* **9**, e2021EF002275 (2021).
15. Emanuel, K. A. Thermodynamic control of hurricane intensity. *Nature* **401**, 665–669 (1999).
16. Lin, I.-I., Wu, C.-C., Pun, I.-F. & Ko, D.-S. Upper-Ocean thermal structure and the Western North Pacific category 5 Typhoons. Part I:

ocean features and the category 5 Typhoons' intensification. *Mon. Weather Rev.* **136**, 3288–3306 (2008).

17. Mainelli, M., DeMaria, M., Shay, L. K. & Goni, G. Application of Oceanic heat content estimation to operational forecasting of recent Atlantic category 5 hurricanes. *Weather Forecast.* **23**, 3–16 (2008).

18. Lin, I. -I., Chen, C., Pun, I., Liu, W. T. & Wu, C. Warm ocean anomaly, air sea fluxes, and the rapid intensification of tropical cyclone Nargis (2008). *Geophys. Res. Lett.* https://doi.org/10.1029/2008GL035815 (2009).

19. Huang, P., Lin, I.-I., Chou, C. & Huang, R.-H. Change in ocean sub-surface environment to suppress tropical cyclone intensification under global warming. *Nat. Commun.* **6**, 7188 (2015).

20. DeMaria, M. The effect of vertical shear on tropical cyclone intensity change. *J. Atmos. Sci.* **53**, 2076–2088 (1996).

21. Frank, W. M. & Ritchie, E. A. Effects of vertical wind shear on the intensity and structure of numerically simulated hurricanes. *Mon. Wea. Rev.* **129**, 2249–2269 (2001).

22. Hendricks, E. A., Peng, M. S., Fu, B. & Li, T. Quantifying environ-mental control on tropical cyclone intensity change. *Mon. Weather Rev.* **138**, 3243–3271 (2010).

23. Shu, S., Ming, J. & Chi, P. Large-scale characteristics and probability of rapidly intensifying tropical cyclones in the Western North Pacific Basin. *Weather Forecast.* **27**, 411–423 (2012).

24. Hill, K. A. & Lackmann, G. M. Influence of environmental humidity on tropical cyclone size. *Mon. Weather Rev.* **137**, 3294–3315 (2009).

25. Patricola, C. M. & Wehner, M. F. Anthropogenic influences on major tropical cyclone events. *Nature* **563**, 339–346 (2018).

26. Guan, S. et al. Ocean internal tides suppress tropical cyclones in the South China Sea. *Nat. Commun.* **15**, 3903 (2024).

27. Wang, H. & Wang, Y. A numerical study of typhoon megi (2010). Part II: eyewall evolution crossing the luzon island. *AMS J.* **149**, 2 (2021).

28. Sun, J., Xu, F., Oey, L.-Y. & Lin, Y. Monthly variability of Luzon Strait tropical cyclone intensification over the Northern South China Sea in recent decades. *Clim. Dyn.* **52**, 3631–3642 (2018).

29. Gray, W. M. Global view of the origin of tropical disturbances and storms. *Mon. Weather Rev.* **96**, 669–700 (1968).

30. Cram, T. A., Persing, J., Montgomery, M. T. & Braun, S. A. A lagrangian trajectory view on transport and mixing processes between the eye, eyewall, and environment using a high-resolution simulation of Hurricane Bonnie (1998). *J. Atmos. Sci.* **64**, 1835–1856 (2007).

31. Zeng, Z., Wang, Y. & Wu, C.-C. Environmental dynamical control of tropical cyclone intensity—an observational study. *Mon. Weather Rev.* **135**, 38–59 (2007).

32. Riemer, M., Montgomery, M. T. & Nicholls, M. E. A new paradigm for intensity modification of tropical cyclones: thermodynamic impact of vertical wind shear on the inflow layer. *Atmos. Chem. Phys.* **10**, 3163–3188 (2010).

33. Tang, B. & Emanuel, K. A ventilation index for Tropical Cyclones. *Bull. Am. Meteorol. Soc.* **93**, 1901–1912 (2012).

34. Li, Z., Yu, W., Li, T., Murty, V. S. N. & Tangang, F. Bimodal character of cyclone climatology in the bay of bengal modulated by monsoon seasonal cycle. *J. Clim.* **26**, 1033–1046 (2013).

35. Chen, X., Wang, Y. & Zhao, K. Synoptic flow patterns and large-scale characteristics associated with rapidly intensifying tropical cyclones in the South China Sea. *Mon. Weather Rev.* **143**, 64–87 (2015).

36. Yang, L. et al. Characteristics of rapidly intensifying tropical cyclones in the South China Sea, 1980–2016. *Adv. Clim. Change Res.* **13**, 333–343 (2022).

37. Potter, H. & Rudzin, J. E. Upper-ocean temperature variability in the gulf of mexico with implications for hurricane intensity. *J. Phys. Oceanogr.* **51**, 10 (2021).

38. Emanuel, K., DesAutels, C., Holloway, C. & Korty, R. Environmental control of tropical cyclone intensity. *J. Atmos. Sci.* **61**, 843–858 (2004).

39. Li, X. et al. Analysis of an ensemble of high-resolution WRF simu-lations for the rapid intensification of super typhoon rammasun (2014). *Adv. Atmos. Sci.* **37**, 187–210 (2020).

40. Huang, Q., Ge, X. & Peng, M. Simulation of rapid intensification of super typhoon lekima (2019). Part I: evolution characteristics of asymmetric convection under upper-level vertical wind shear. *Front. Earth Sci.* https://doi.org/10.3389/feart.2021.739507 (2021).

41. Liu, K. S. & Chan, J. C. L. Inter-decadal variability of the location of maximum intensity of category 4–5 typhoons and its implication on landfall intensity in East Asia. *Int. J. Climatol.* **39**, 1839–1852 (2018).

42. Zhao, H. & Wu, L. Inter-decadal shift of the prevailing tropical cyclone tracks over the western North Pacific and its mechanism study. *Meteorol. Atmos. Phys.* **125**, 89–101 (2014).

43. Lee, T.-C., Knutson, T. R., Nakaegawa, T., Ying, M. & Cha, E. J. Third assessment on impacts of climate change on tropical cyclones in the Typhoon committee region – part I: observed changes, detec-tion and attribution. *Trop. Cyclone Res. Rev.* **9**, 1–22 (2020).

44. Kossin, J. P., Emanuel, K. A. & Camargo, S. J. Past and projected changes in western north pacific tropical cyclone exposure. *J. Clim.* **29**, 5725–5739 (2016).

45. Zhan, R. & Wang, Y. Weak tropical cyclones dominate the poleward migration of the annual mean location of lifetime maximum inten-sity of northwest pacific tropical cyclones since 1980. *J. Clim.* **30**, 6873–6882 (2017).

46. Kossin, J. P., Emanuel, K. A. & Vecchi, G. A. The poleward migration of the location of tropical cyclone maximum intensity. *Nature* **509**, 349–352 (2014).

47. Murakami, H. & Wang, B. Patterns and frequency of projected future tropical cyclone genesis are governed by dynamic effects. *Com-mun. Earth Environ.* **3**, 1–10 (2022).

48. Emanuel, K. A. Downscaling CMIP5 climate models shows increased tropical cyclone activity over the 21st century. *Proc. Natl. Acad. Sci. USA.* **110**, 12219–12224 (2013).

49. Sugi, M., Murakami, H. & Yoshida, K. Projection of future changes in the frequency of intense tropical cyclones. *Clim. Dyn.* **49**, 619–632 (2016).

50. Shen, W., Tuleya, R. E. & Ginis, I. A sensitivity study of the thermo-dynamic environment on GFDL model hurricane intensity: impli-cations for global warming. *J. Clim.* **13**, 109–121 (2000).

51. Nakamura, R., Shibayama, T., Esteban, M. & Iwamoto, T. Future typhoon and storm surges under different global warming sce-narios: case study of typhoon Haiyan (2013). *Nat. Hazards* **82**, 1645–1681 (2016).

52. Zhang, G., Murakami, H., Knutson, T. R., Mizuta, R. & Yoshida, K. Tropical cyclone motion in a changing climate. *Sci. Adv.* **6**, 17 (2020).

53. Wang, S. & Toumi, R. Recent migration of tropical cyclones toward coasts. *Science* **371**, 514–517 (2021).

54. Wang, C. & Wu, L. Influence of future tropical cyclone track chan-ges on their basin-wide intensity over the western north pacific: downscaled CMIP5 projections. *Adv. Atmos. Sci.* **32**, 613–623 (2015).

55. Tsuboki, K. et al. Future increase of supertyphoon intensity asso-ciated with climate change. *Geophys. Res. Lett.* **42**, 646–652 (2015).

56. Liu, L., Wang, Y., Zhan, R., Xu, J. & Duan, Y. Increasing destructive potential of landfalling tropical cyclones over China. *J. Clim.* **33**, 3731–3743 (2020).

57. Knapp, K. R., Kruk, M. C., Levinson, D. H., Diamond, H. J. & Neumann, C. J. The international best track archive for climate stewardship (IBTrACS). *Bull. Am. Meteor. Soc.* **91**, 363–376 (2010).

58. Hersbach, H. et al. The ERA5 global reanalysis. *Quart. J. R. Meteor. Soc.* **146**, 1999–2049 (2020).

59. Reynolds, R. W. et al. Daily high-resolution-blended analyses for sea surface temperature. *J. Clim.* **20**, 5473–5496 (2007).

60. Eyring, V. et al. Overview of the coupled model intercomparison project phase 6 (CMIP6) experimental design and organization. *Geosci. Model Dev.* **9**, 1937–1958 (2016).

61. Meinshausen, M. et al. The shared socio-economic pathway (SSP) greenhouse gas concentrations and their extensions to 2500. *Geosci. Model Dev.* **13**, 3571–3605 (2020).

62. Knapp, K. R. & Kruk, M. C. Quantifying interagency differences in tropical cyclone best-track wind speed estimates. *Mon. Weather Rev.* **138**, 1459–1473 (2010).

63. Schreck, C. J., Knapp, K. R. & Kossin, J. P. The impact of best track discrepancies on global tropical cyclone climatologies using IBTrACS. *Mon. Weather Rev.* **142**, 3881–3899 (2014).

64. Emanuel, K. A. Sensitivity of tropical cyclones to surface exchange coefficients and a revised steady-state model incorporating eye dynamics. *J. Atmos. Sci.* **52**, 3969–3976 (1995).

65. Bister, M. & Emanuel, K. A. Dissipative heating and hurricane intensity. *Meteor. Atmos. Phys.* **65**, 233–240 (1998).

66. Bister, M. & Emanuel, K. A. Low frequency variability of tropical cyclone potential intensity 1. Interannual to interdecadal variability. *J. Geophys. Res.* **107**, ACL 26-1–ACL 26-15 (2002).

67. Emanuel, K., Ravela, S., Vivant, E. & Risi, C. A statistical deterministic approach to hurricane risk assessment. *Bull. Am. Meteor. Soc.* **87**, 299–314 (2006).

68. Zhu, Y. et al. Factors affecting climate variability of basin-wide western North Pacific tropical cyclone intensity. *Int. J. Climatol.* **43**, 1448–1460 (2022).

69. Wu, L., Wang, R. & Feng, X. Dominant role of the ocean mixed layer depth in the increased proportion of intense typhoons during 1980–2015. *Earth's Future* **6**, 1518–1527 (2018).

70. Edson, J. B. et al. On the exchange of momentum over the open ocean. *J. Phys. Oceanogr.* **43**, 1589–1610 (2013).

Acknowledgements

Author contributions

W.D.Y., T.M. and S.S. conceived the project. T.M. analyzed the data and generated the figures. T.M. improved and ran the tropical cyclone intensity model with assistance from H.K.Z. and L.G.W. T.M. ran the WRF model with help from R.X., W.D.Y. and S.S. TM wrote the main manuscript, with further inputs from W.D.Y., S.S. and H.L. W.D.Y., S.S., H.K.Z., R.X., H.L. and L.G.W. contributed to the discussion of the results and provided comments on the manuscript.

Competing interests

The authors declare no competing interests.

Additional information

Supplementary information The online version contains supplementary material available at https://doi.org/10.1038/s41467-025-62334-4.

Correspondence and requests for materials should be addressed to Wei-Dong Yu.

Peer review information *Nature Communications* thanks Ralf Toumi, and the other, anonymous, reviewer(s) for their contribution to the peer review of this work. A peer review file is available.

Reprints and permissions information is available at http://www.nature.com/reprints

Publisher's note Springer Nature remains neutral with regard to jurisdictional claims in published maps and institutional affiliations.